Int J Fract (2011) 167:15–31
DOI 10.1007/s10704-010-9513-6

ORIGINAL PAPER

Modeling of cohesive crack growth in partially saturated porous media; a study on the permeability of cohesive fracture

O. R. Barani · A. R. Khoei · M. Mofid

Received: 29 January 2010 / Accepted: 2 June 2010 / Published online: 24 June 2010

Abstract Modeling the water flow in cohesive fracture is a fundamental issue in the crack growth simulation of cracked concrete gravity dams and hydraulic fracture problems. In this paper, a mathematical model is presented for the analysis of fracture propagation in the semi-saturated porous media. The solid behavior incorporates a discrete cohesive fracture model, coupled with the flow in porous media through the fracture network. The double-nodded zero-thickness cohesive interface element is employed for the mixed mode fracture behavior in tension and contact behavior in compression. The modified crack permeability is applied in fracture propagation based on the data obtained from experimental results to implement the roughness of fracture walls.

Keywords Fracture propagation · Porous media · Partially saturated · Cohesive fracture · Fracture permeability

1 Introduction

Modeling the water flow in cohesive fracture propagation plays the main role in the crack growth simulation of porous saturated media. The hydraulic fracture problem and cracked concrete gravity dams normally have cracks in practical service due to previous earthquakes, construction conditions, or temperature effects. For a concrete dam subjected to its probable maximum flood, it is speculated that the hydrostatic pressure acting inside the crack induces additional material damage and hence, reduce the resistance against further cracking which can lead to the weakness of structure and the penetration of water that exerts uplift pressure (Rescher 1990; Zhu and Pekau 2007). The study of crack propagation in concrete dams can be performed based on the development of interface models in poroelastic material.

Modeling of discontinuities between two bodies in contact has been performed by contact elements in computational solid mechanics. The idea has been used to model the cohesive forces via the cohesive elements in numerical fracture mechanics (Ortiz and Suresh 1993; Xu and Needleman 1994). The double-nodded zero-thickness interface element was used by Ng and Small (1997) in flow problems. Segura and Carol (2004) proposed the influence of transversal conductivity with the aim of applying these elements in the hydro-mechanical problems. Simoni and Secchi (2003) implemented the double-nodded interface elements in quasi-static fracture propagation of saturated porous media. The technique was proposed by Schrefler et al. (2006) and Secchi et al. (2007) based on an adaptive mesh refinement in porous materials. The cohesive crack growth was performed by Khoei et al. (2009) using the adaptive FE strategy in the framework of

O. R. Barani · A. R. Khoei (✉) · M. Mofid
Center of Excellence in Structures and Earthquake Engineering, Department of Civil Engineering, Sharif University of Technology, P.O. Box. 11365-9313, Tehran, Iran
e-mail: arkhoei@sharif.edu

cohesive interface elements. A new formulation was developed for double-nodded interface elements by Khoei et al. (2010) in the dynamic fracture propagation of saturated porous media, in which a new transversal conductivity relation was introduced.

As the fracture mechanics–based analysis is being increasing accepted as an analytical and numerical tool for cracked massive concrete structures, the fracture properties must be defined appropriately according to experimental data. Brühwiler and Saoma (1995a,b) conducted a series of experimental studies to determine that the static pressure inside a crack is a function of crack opening and that, along the fracture process zone, this pressure reduces from full reservoir pressure to zero. Reinhardt et al. (1998) investigated the flow in concrete cracks and concluded that the permeability of cracks having an opening more than about 0.04 mm is higher than the undamaged concrete. For smaller crack widths the penetration behavior is similar to that of uncracked concrete. Slowik and Saouma (2000) developed an experimental and numerical investigation on the influence of water pressure on crack propagation in concrete. From the experimental results they pointed out that the crack opening rate significantly influences the water pressure distribution. On the basis of experimental results they proposed an interface model, considering the fluid permeability as a function of crack opening displacements. However they did not consider the compressibility of solid and fluid and also the roughness of fracture walls as a key parameter of fracture permeability. That is a general assumption for the concrete material that a properly cured concrete or an underwater concrete is fully saturated by water. Persson (1997) indicated that the relative humidities inside concrete samples are lower than 100% even though the samples were stored under water indicating unsaturated states of concrete. It was shown that the relative humidity could be about 0.77 even after 450 days under water curing.

In the present paper, a finite element algorithm was presented for the numerical modeling of cohesive fracture in a partially saturated porous media. The double-nodded zero-thickness cohesive interface elements were employed to capture the mixed mode fracture behavior in tension and compression. In order to describe the behavior of fractured media, two equilibrium equations were applied similar to those employed for the mixture of solid–fluid phase in semi-saturated media, including: the momentum balance of fractured media, and the balance of fluid mass within the fracture. Based on the experimental data performed by Slowik and Saouma (2000), a modified crack permeability is introduced to model the roughness of fracture walls.

2 FE formulation of semi-saturated porous media

The mathematical formulation governing the behavior of dynamic saturated porous medium was first introduced by Biot (1941). The first numerical solution for these equations was made by Ghaboussi and Wilson (1973) . A simple extension of two phase formulation to semi-saturated problems was proposed by Zienkiewicz et al. (1990) based on the assumption of the air or gas present in the pores remaining at atmospheric pressure. They employed their extended formulation for the dynamic analysis of a semi-saturated dam under earthquake loading. The coupled formulations that involve the air and water phases in a porous medium have been presented by Alonso et al. (1990) and Gawin and Schrefler (1996). However, because of great complexity of three-phase models, an extensive and special designed testing is required to determine the properties of the matrix–air–water mixture.

In the theory of porous media, the effective stress is an essential concept for the deformation of solid skeleton. The effective stress σ'_{ij} can be defined by $\sigma'_{ij} = \sigma_{ij} - \alpha\delta_{ij}S_w p_w$, in which δ_{ij} denotes the Kronecker delta and σ_{ij} and p_w are the total stress and water pressure, respectively, with positive value in compression. In this relation, α is the Biot coefficient which depends on the material type and defined as $\alpha = 1 - K_T/K_s$, with K_T and K_s denoting the bulk modulus of porous medium and solid particles, respectively. S_w is the water saturation, defined as a function of the water pressure, i.e. $S_w = S_w(p_w)$. Note that for the saturated porous media, the water pressure is assumed to be positive and the effective stress is less than the total stress, while for the partially saturated porous medium when the gas pressure is close to zero, the water pressure is negative and the effective stress is more than the total stress.

The linear momentum balance for the mixture of solid–fluid phase can be written as

$$\sigma_{ij,j} + \rho\ddot{u}_i - \rho b_i = 0 \tag{1}$$

where b_i is the body force per unit mass and ρ indicates the density of total mixture defined by $\rho = nS_w\rho_w + (1-n)\rho_s$, with ρ_w denoting the water density, ρ_s the density of solid particles, and n the porosity.

Incorporating the Darcy law, the mass balance for the fluid phase can be written as

$$\left(k_{rm}k_{ij}(p_{w,j}+\rho_w\ddot{u}_j-\rho_w b_j)\right)_{,i}+\alpha S_w\dot{\varepsilon}_{ii}+\frac{\dot{p}_w}{Q^*}=0 \tag{2}$$

where ε_{ii} is the total volumetric strain, k_{ij} the permeability tensor of the medium, k_{rm} the relative permeability of the matrix which is a function of the water pressure, i.e. $k_{rm}=k_{rm}(p_w)$, and Q^* is defined as

$$\frac{1}{Q^*}=C_s+n\frac{S_w}{K_w}+(\alpha-n)\frac{S_w}{K_s}\left(S_w+\frac{C_s}{n}p_w\right) \tag{3}$$

where K_w denoting the bulk modulus for liquid phase and C_s the specific moisture content defined as ndS_w/dp_w (Zienkiewicz et al. 1999).

The governing Eqs. (1) and (2) can be discretized for quasi-static problems in the absence of acceleration terms by using two sets of shape functions $\mathbf{N}_u$ and $\mathbf{N}_p$ for two variables u_i and p_w, defined as $\mathbf{u}=\mathbf{N}_u\bar{\mathbf{u}}$ and $p_w=\mathbf{N}_p\bar{p}_w$, based on the standard Galerkin technique to transform these equations into a set of algebraic equations as (Khoei et al. 2004)

$$\mathbf{K}\bar{\mathbf{u}}-\mathbf{Q}\bar{p}_w=\mathbf{f}^{(1)} \tag{4}$$

$$\mathbf{Q}\dot{\bar{\mathbf{u}}}+\mathbf{H}\bar{p}_w+\mathbf{G}\dot{\bar{p}}_w=\mathbf{f}^{(2)} \tag{5}$$

where the stiffness matrix $\mathbf{K}$, the coupling matrix $\mathbf{Q}$, the permeability matrix $\mathbf{H}$, and the compressibility matrix $\mathbf{G}$ are defined as

$$\begin{aligned}
\mathbf{K}&=\int_\Omega \mathbf{B}^T\mathbf{D}\mathbf{B}\,d\Omega\\
\mathbf{Q}&=\int_\Omega \mathbf{B}^T S_w\alpha\mathbf{m}\mathbf{N}_p\,d\Omega\\
\mathbf{H}&=\int_\Omega \nabla\mathbf{N}_p^T\mathbf{k}k_{rm}\nabla\mathbf{N}_p\,d\Omega\\
\mathbf{G}&=\int_\Omega \mathbf{N}_p^T\frac{1}{Q^*}\mathbf{N}_p\,d\Omega
\end{aligned} \tag{6}$$

and

$$\begin{aligned}
\mathbf{f}^{(1)}&=\int_\Omega \mathbf{N}_u^T\rho\mathbf{b}\,d\Omega+\int_{\Gamma_t}\mathbf{N}_u^T\bar{\mathbf{t}}d\Gamma\\
\mathbf{f}^{(2)}&=-\int_\Omega \mathbf{N}_p^T\nabla^T(\mathbf{k}k_{rm}\rho_w\mathbf{b})\,d\Omega+\int_{\Gamma_q}\mathbf{N}_p^T\frac{q_w}{\rho_w}d\Gamma
\end{aligned} \tag{7}$$

where $\mathbf{B}$ is the matrix relating the increments of strain and displacements, $\mathbf{D}$ is the material property matrix of solid skeleton, and $\mathbf{m}$ is defined as $\mathbf{m}=[1,1,0]^T$ (Khoei et al. 2006). In above relations, Ω is the domain of fluid and solid fields, Γ_t is the external boundary for traction, Γ_q is the external boundary for influx, and q_w is the imposed flux on Γ_q. The permeability matrix $\mathbf{k}$ is defined as

$$\mathbf{k}=\begin{bmatrix}k_x & k_{xy}\\ k_{yx} & k_y\end{bmatrix} \tag{8}$$

where k_x and k_y are the permeability coefficients in x and y directions, respectively, and k_{xy} and k_{yx} are generally set to zero.

Based upon the pore network model, a relationship between the capillary pressure and the water saturation is proposed by van Genuchten (1980) as

$$S_w(p_w)=\left[1+\left(\frac{p_w}{p_r}\right)^{1/(1-m)}\right]^{-m} \tag{9}$$

in which the reference pressure p_r and the coefficient m are defined based on the experimental data obtained by Baroghel-Bouny et al. (1999) as $p_r=18.6237$ MPa and $m=0.4396$, respectively. The relative permeability is defined for soils by van Genuchten (1980) as

$$k_{rm}(S_w)=\sqrt{S_w}[1-(1-S_w^{1/m})^m]^2 \tag{10}$$

The applicability of above relation in modeling of moisture transport in unsaturated concrete is shown by Savage and Janssen (1997).

3 Mechanical behavior of fractured media

A convenient model to describe the mechanical behavior of fracture in quasi-brittle materials is based on the cohesive fracture model, originally introduced by Dugdale (1960) and Barenblatt (1962) and has since been used by many researchers to describe the near–tip nonlinear zone for cracks. Generally, the fracture process zone (FPZ) is a nonlinear zone characterized by progressive softening, where the traction across the forming crack surface decreases as separation increases. It was shown that the fracture process of concrete can be characterized by the strain softening and fracture toughening due to the formation and branching of micro-cracks (Shum and Hutchinson 1990; Jenq and Shah 1991). During the fracture process, the high-stress state near the crack tip causes micro-cracking at flaw sites, such as pores and air voids. This micro-cracking phenomenon consumes a part of the external

energy introduced by the applied load, and the resulting micro-cracks can be produced with respect to the main crack plane. Furthermore, the density of micro-cracks generally decreases with increasing the distance from the face of main crack, however, some micro-cracks may be arrested by the aggregates and air voids.

The crack branching may occur as a higher level of load is applied. When the load reaches the critical level, the macro-crack starts initiating and propagating, and finally breaks the concrete. The fracture toughening can be happened due to micro-cracks. The crack deflection occurs when a relatively stronger particle is located in the pathway of main crack. The grain bridging occurs when the crack has advanced beyond an aggregate that continues to transmit stresses across the cracks until it ruptures or is pulled out. The crack may propagate into several branches due to heterogeneity of concrete, and more energy must be consumed to form new crack branches. Generally, the crack surface is a tortuous path due to toughening mechanism, in which the crack generally branch around aggregates, causing random propagation in concrete. During the opening of a tortuous crack there may be some frictional sliding between the cracked faces that causes energy dissipation. The crack bridging and crack blunting may occur due to aggregates and air voids in the pathway of the main crack (Bazant and Planas 1998). The width and micro-cracking density distribution at the fracture front may vary depending on the structure size, shape, and type of loading. Owing to the stiffer matrix compared to fractures, most deformation in process zone occurs in the fractures, in the form of normal and shear displacement. As a result, the existing fractures may open, grow, or even induce new ones.

The first implementation of cohesive fracture model in the finite element algorithm was performed by Hilleborg et al. (1976). They extended the concept of cohesive crack for concrete by proposing that the cohesive crack may be assumed to develop anywhere, even if no pre-existing macro-crack is actually present, called as the fictitious crack model. Ortiz and Suresh (1993) and Xu and Needleman (1994) proposed the cohesive model to evaluate the cohesive forces in numerical fracture mechanics. A fracture criterion was proposed by Camacho and Ortiz (1996) for the mixed mode fracture and widely used in literature. The cohesive fracture model has been widely used in fracture mechanics problems, including: the quasi-static crack propagation of saturated porous media by Simoni and Secchi (2003), Schrefler et al. (2006) and Secchi et al. (2007), the cohesive crack growth of brittle materials by Song et al. (2006), Birgisson et al. (2008) and Khoei et al. (2009), and the dynamic fracture propagation of saturated porous media by Khoei et al. (2010).

3.1 Formulation of cohesive fracture zone

The fracturing material in the zone of fractured media undergoes the mixed mode crack opening, in which the crack moves along an interface separating two solid components. The mixed cohesive model involves the simultaneous activation of normal and tangential displacement discontinuity with respect to the crack and corresponding tractions. In this model, the effective traction t_e is resolved into the normal and tangential components, i.e. t_n and t_s, in which $t_e = \sqrt{t_n^2 + t_s^2}$. In similar manner, the effective displacement is defined by $\delta_e = \sqrt{\delta_n^2 + \delta_s^2}$, where δ_n and δ_s are the normal displacement and shear sliding of fracture surfaces. The non-dimensional effective displacement can be defined as $\lambda_e = \sqrt{(\delta_n/\delta_c)^2 + (\delta_s/\delta_c)^2}$, in which δ_c denotes the critical displacement where complete separation, i.e. zero traction, occurs. In Fig. 1, the bilinear cohesive law is shown in terms of the normalized effective traction and normalized effective displacement. The pre-peak region represents the elastic part of the intrinsic cohesive law whereas the softening portion after the peak load accounts for the damage occurring in the fracture process zone. The parameter λ_{cr} is a non-dimensional displacement, which is defined to adjust the pre-peak slope of the cohesive law, and is set to a small value to obtain more exact results. The normal and shear tractions are defined as (Song et al. 2006)

$$\begin{aligned} t_n &= \frac{\sigma_c}{\lambda_{cr}}\left(\frac{\delta_n}{\delta_c}\right) && \text{if } \lambda_e < \lambda_{cr} \\ t_n &= \frac{\sigma_c}{\lambda_e}\frac{1-\lambda_e}{1-\lambda_{cr}}\left(\frac{\delta_n}{\delta_c}\right) && \text{if } \lambda_e > \lambda_{cr} \text{ (loading)} \\ t_n &= \frac{\sigma_c}{\lambda_{e1}}\frac{1-\lambda_{e1}}{1-\lambda_{cr}}\left(\frac{\delta_n}{\delta_c}\right) && \text{if } \lambda_e > \lambda_{cr} \text{ (unloading)} \end{aligned} \tag{11}$$

and

$$\begin{aligned} t_s &= \frac{\sigma_c}{\lambda_{cr}}\left(\frac{\delta_s}{\delta_c}\right) && \text{if } \lambda_e < \lambda_{cr} \\ t_s &= \frac{\sigma_c}{\lambda_e}\frac{1-\lambda_e}{1-\lambda_{cr}}\left(\frac{\delta_s}{\delta_c}\right) && \text{if } \lambda_e > \lambda_{cr} \text{ (loading)} \\ t_s &= \frac{\sigma_c}{\lambda_{e1}}\frac{1-\lambda_{e1}}{1-\lambda_{cr}}\left(\frac{\delta_s}{\delta_c}\right) && \text{if } \lambda_e > \lambda_{cr} \text{ (unloading)} \end{aligned} \tag{12}$$

where σ_c is the material strength and λ_{e1} is the non-dimensional displacement just before unloading.

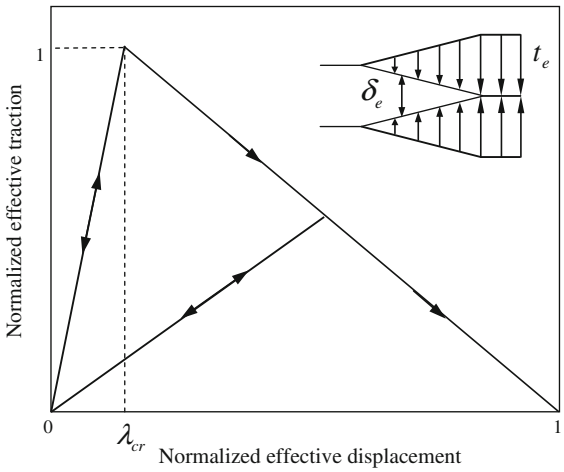

Fig. 1 A bilinear cohesive law in terms of normalized effective displacement and normalized effective traction

In order to derive the components of cohesive material matrix $\mathbf{C}_f$ for the fractured zone, it needs to differentiate tractions with respect to the normal and shear displacements (Khoei et al. 2010). Hence, the components of cohesive material matrix $\mathbf{C}_f$ can be defined as

$$\mathbf{C}_f = \begin{bmatrix} C_{ss} & C_{sn} \\ C_{ns} & C_{nn} \end{bmatrix} = \begin{bmatrix} \frac{\partial t_s}{\partial \delta_s} & \frac{\partial t_s}{\partial \delta_n} \\ \frac{\partial t_n}{\partial \delta_s} & \frac{\partial t_n}{\partial \delta_n} \end{bmatrix} \tag{13}$$

Substituting relations (11) and (12) into (13), the cohesive material matrix can be obtained as

$$\mathbf{C}_f = \begin{bmatrix} \frac{\sigma_c}{\lambda_{cr}\delta_c} & 0 \\ 0 & \frac{\sigma_c}{\lambda_{cr}\delta_c} \end{bmatrix} \quad \text{if } \lambda_e < \lambda_{cr}$$

$$\mathbf{C}_f = \begin{bmatrix} -\frac{\delta_c\sigma_c}{1-\lambda_{cr}}\left(\frac{\delta_s}{\lambda_e\delta_c^2}\right)^2 + (1-\lambda_e)\frac{\delta_c\sigma_c}{1-\lambda_{cr}}\left(\frac{1}{\lambda_e\delta_c^2} - \frac{1}{\lambda_e^3}\frac{\delta_s^2}{\delta_c^4}\right) & -\frac{\delta_c\sigma_c}{1-\lambda_{cr}}\frac{1}{\lambda_e^3}\left(\frac{\delta_s}{\delta_c^2}\right)\left(\frac{\delta_n}{\delta_c^2}\right) \\ -\frac{\delta_c\sigma_c}{1-\lambda_{cr}}\frac{1}{\lambda_e^3}\left(\frac{\delta_s}{\delta_c^2}\right)\left(\frac{\delta_n}{\delta_c^2}\right) & -\frac{\delta_c\sigma_c}{1-\lambda_{cr}}\left(\frac{\delta_n}{\lambda_e\delta_c^2}\right)^2 + (1-\lambda_e)\frac{\delta_c\sigma_c}{1-\lambda_{cr}}\left(\frac{1}{\lambda_e\delta_c^2} - \frac{1}{\lambda_e^3}\frac{\delta_n^2}{\delta_c^4}\right) \end{bmatrix}$$

$$\text{if } \lambda_e > \lambda_{cr} \text{ (loading)}$$

$$\mathbf{C}_f = \begin{bmatrix} \frac{\sigma_c}{\delta_c}\left(\frac{1-\lambda_{e1}}{1-\lambda_{cr}}\right)\frac{1}{\lambda_{e1}} & 0 \\ 0 & \frac{\sigma_c}{\delta_c}\left(\frac{1-\lambda_{e1}}{1-\lambda_{cr}}\right)\frac{1}{\lambda_{e1}} \end{bmatrix} \quad \text{if } \lambda_e > \lambda_{cr} \text{ (unloading)} \tag{14}$$

If the normal component of traction is in compression, i.e. $t_n < 0$ and $\delta_n = 0$, the cohesive shear traction t_{sC} can be defined according to relations (12) as

$$\begin{aligned} t_{sC} &= \frac{\sigma_c}{\lambda_{cr}}\left(\frac{\delta_s}{\delta_c}\right) && \text{if } \lambda_e < \lambda_{cr} \\ t_{sC} &= \frac{\sigma_c}{\lambda_e}\frac{1-\lambda_e}{1-\lambda_{cr}}\left(\frac{\delta_s}{\delta_c}\right) && \text{if } \lambda_e > \lambda_{cr} \text{ (loading)} \\ t_{sC} &= \frac{\sigma_c}{\lambda_{e1}}\frac{1-\lambda_{e1}}{1-\lambda_{cr}}\left(\frac{\delta_s}{\delta_c}\right) && \text{if } \lambda_e > \lambda_{cr} \text{ (unloading)} \end{aligned} \tag{15}$$

and the non-dimensional effective displacement is defined as $\lambda_e = |\delta_s/\delta_c|$. In this case, the shear traction can be computed by $|t_s| = |t_{sC}| + \mu\,|t_n|$, with μ denoting the friction coefficient.

4 FE formulation of fractured media

In order to perform the finite element model of fractured media, two equilibrium equations are implemented similar to those presented in Sect. 2 for the mixture of solid–fluid phase. The first equation deals with the mechanical behavior of fracture, while the second equation describes the balance of fluid mass within the fracture. The momentum balance of fractured media can be written according to cohesive fracture behavior similar to Eq. (1) as

$$\sigma_{ij,j} + \rho_f \ddot{u}_i - \rho_f b_i = 0 \tag{16}$$

The balance of fluid mass within the fracture zone can be rewritten according to Eq. (2) for the fractured media as

$$\left(k_{rf}(k_f)_{ij}(p_{w,j} + \rho_w \ddot{u}_j - \rho_w b_j)\right)_{,i} + S_w\frac{\dot{w}}{w} + \frac{\dot{p}_w}{Q_f^*} = 0 \tag{17}$$

where $\dot{w}$ is the rate of fracture aperture, Q_f^* is defined as $1/Q_f^* = nS_w/K_w$, $\rho_f = nS_w\rho_w$, k_{rf} is the relative permeability of fracture, and $(k_f)_{ij}$ is the fracture permeability tensor.

Applying the standard finite element Galerkin discretization process to the weak form of Eqs. (16) and (17), the FE formulation of fractured media for quasi-static condition in the absence of acceleration terms can be written similar to Eqs. (4) and (5) as

$$\mathbf{K}_f\bar{\mathbf{u}} - \mathbf{Q}_f\bar{p}_w = \mathbf{f}_f^{(1)} \tag{18}$$

$$\mathbf{Q}_f\bar{\mathbf{u}} + \mathbf{H}_f\bar{p}_w + \mathbf{G}_f\dot{\bar{p}}_w = \mathbf{f}_f^{(2)} \tag{19}$$

where the cohesive stiffness matrix $\mathbf{K}_f$, the coupling matrix $\mathbf{Q}_f$, the permeability matrix $\mathbf{H}_f$, and the compressibility matrix $\mathbf{G}_f$ for the fractured zone are defined similar to the semi-saturated porous media as

$$\begin{aligned}
\mathbf{K}_f &= \int_\Omega \mathbf{B}_f^T\mathbf{D}_f\mathbf{B}_f\, d\Omega \\
\mathbf{Q}_f &= \int_\Omega \mathbf{B}_f^T S_w\mathbf{m}_f\mathbf{N}_f\, d\Omega \\
\mathbf{H}_f &= \int_\Omega \nabla\mathbf{N}_f^T\mathbf{k}_f k_{rf}\nabla\mathbf{N}_f\, d\Omega \\
\mathbf{G}_f &= \int_\Omega \mathbf{N}_f^T\frac{1}{Q_f^*}\mathbf{N}_f\, d\Omega
\end{aligned} \tag{20}$$

and

$$\begin{aligned}
\mathbf{f}_f^{(1)} &= \int_\Omega \mathbf{N}_f^T\rho_f\mathbf{b}\; d\Omega \\
\mathbf{f}_f^{(2)} &= -\int_\Omega \mathbf{N}_f^T\nabla^T(\mathbf{k}_f k_{rf}\rho_w\mathbf{b})\, d\Omega
\end{aligned} \tag{21}$$

where $\mathbf{D}_f = w\mathbf{C}_f$, with w denoting the fracture width and the cohesive material matrix $\mathbf{C}_f$ is defined in relations (14).

The stiffness matrix of cohesive fracture elements can be obtained based on the standard contact elements extensively used in literature (Khoei 2005). The relative displacements at any points along the fracture element, as shown in Fig. 2, are given by $\boldsymbol{\delta} = \mathbf{u}_{\text{top}} - \mathbf{u}_{\text{bot}}$, in which $\boldsymbol{\delta} = \langle\delta_s, \delta_n\rangle^T$ and $\mathbf{u} = \langle u_s, u_n\rangle^T$ with $(u_s)_{\text{top}}$ and $(u_n)_{\text{top}}$ denoting the displacements in the local s and n directions of the top side of element, and $(u_s)_{\text{bot}}$ and $(u_n)_{\text{bot}}$ the displacements in the local s and n directions of the bottom side of element, respectively. The relative displacements at any point of the element can be related to the nodal values by $\boldsymbol{\delta} = \mathbf{N}_f\bar{\mathbf{u}}$,

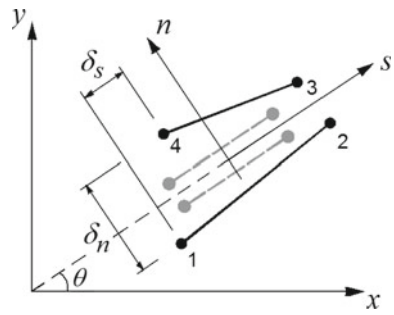

Fig. 2 Schematic drawing of zero thickness double-noded interface element

with $\mathbf{N}_f = \langle -(\mathbf{N}_f)_{\text{bot}}, (\mathbf{N}_f)_{\text{top}}\rangle$ and $\bar{\mathbf{u}} = \langle\bar{\mathbf{u}}_{\text{bot}}, \bar{\mathbf{u}}_{\text{top}}\rangle^T$. In this relation, N_f is the shape functions of cohesive fracture element defined by $(\mathbf{N}_f)_{\text{bot}} = \langle\mathbf{N}_{f1}, \mathbf{N}_{f2}\rangle$ and $(\mathbf{N}_f)_{\text{top}} = \langle\mathbf{N}_{f3}, \mathbf{N}_{f4}\rangle$. The shear and normal strains, i.e. $\boldsymbol{\varepsilon} = \{\gamma, \varepsilon_n\}$, can be obtained from the relative displacements as $\gamma = \frac{1}{w}\delta_s$ and $\varepsilon_n = \frac{1}{w}\delta_n$. Hence, the strain vector can be defined as $\boldsymbol{\varepsilon} = \mathbf{B}_f\bar{\mathbf{u}}$, where the $\mathbf{B}_f$ matrix is equal to $\frac{1}{w}\mathbf{N}_f$.

In relations (20) and (21), $\mathbf{m}_f = [1, 0]^T$ and $\nabla\mathbf{N}_f$ is defined as

$$\nabla\mathbf{N}_f = \begin{bmatrix} \dfrac{\partial N_{f1}}{\partial s} & \dfrac{\partial N_{f2}}{\partial s} & \dfrac{\partial N_{f3}}{\partial s} & \dfrac{\partial N_{f4}}{\partial s} \\ -\dfrac{N_{f1}}{w} & -\dfrac{N_{f2}}{w} & \dfrac{N_{f3}}{w} & \dfrac{N_{f4}}{w} \end{bmatrix} \tag{22}$$

and $\mathbf{k}_f$ is the fracture permeability matrix defined as

$$\mathbf{k}_f = \begin{bmatrix} k_l & 0 \\ 0 & k_n \end{bmatrix} \tag{23}$$

where k_l is the longitudinal permeability coefficient, k_n is the transverse permeability coefficient, and the relative permeability of fracture is assumed to be $k_{rf} = 1$ (Meschke and Grasberger 2003).

4.1 Fracture permeability coefficient

In order to model the fluid flow through the discontinuity, the zero-thickness elements have been widely used in literature, which can be classified into the single, double and triple-nodded elements. The single-nodded elements are the simplest one, which are superimposed onto the standard continuum mesh. The triple-nodded elements are used to model the influence of a transversal conductivity through the discontinuity appropriately (Guiducci et al. 2002). In these elements, the two nodes of adjacent continuum elements represent the

potentials in the pore system on each side of the interface, and the third node in the middle represents the average potential of fluid in the channel represented by the discontinuity. However, the double-nodded interface elements have the advantage of making it possible to use similar FE mesh for both mechanical and fluid flow analyses (Segura and Carol 2004). In the case that the influence of a transversal conductivity is not considered, these elements are similar to the single nodded type although they are geometrically double-nodded, and when the time comes to solve the system, the two nodes must have the same potential. This limitation may, however, be avoided by assuming that the potential in the channel is the average of two sides of the interface. Based on this simple assumption, an alternative flow interface model has been recently developed by Khoei et al. (2010), which preserves both longitudinal and transversal conductivities.

The existence of fracture besides the longitudinal conductivity may also represent an obstacle for fluid flow in the transversal direction because of the potential drop due to the transition from a pore system into an open channel and back into a pore system. Thus, defining the flow potential Φ equal to $p + \rho_w(\ddot{u} - b)z$, with z denoting the distance from a datum, a jump is admitted in the total flow potential field across the fracture related to transverse fluid flux q_t travelling normal to the discontinuity. Considering a discrete version of the Darcy law, in which the total flow potential drop plays the role of total flow potential gradient, the transverse fluid flux is linked to the difference of hydraulic potentials between the two surfaces defining the discontinuity by $q_t = k_t(\Phi^- - \Phi^+)$, where k_t is a transverse hydraulic permeability coefficient and the superscripts $-$ and $+$ stand for each side of the discontinuity (Segura and Carol 2004). In fact, it can be concluded that the single-nodded interfaces are equivalent to the double-nodded and triple-nodded elements with $k_t = \infty$, i.e. the infinite transversal conductivity.

It is desirable to implement the inactive cohesive interface elements in both mechanical and fluid flow media before the critical stress is reached. In fact, an infinite initial stiffness provides a rigid inactive element for mechanical part before the maximum tensile stress is reached. Also, assuming an infinite transversal conductivity and zero longitudinal conductivity lead to inactive elements for flow part before stress reaches the tensile strength of media. Comparing the transverse permeability coefficient k_n with the permeability coefficient k_t introduced by Segura and Carol (2004) , it can be concluded that $k_t = k_n/w$, which leads to inactive cohesive elements for fluid flow before stress reaches the tensile strength of material at that point. However, in order to avoid the numerical difficulty, when aperture is zero an initial large value of k_t is assumed instead of k_n/w.

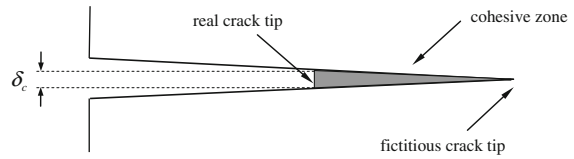

Fig. 3 Schematic description of a cohesive zone model

In order to model the longitudinal permeability, the fractured zone is decomposed into two portions; one is related to the cohesive area and the other is related to the real cracked zone where the cohesive forces are zero (Fig. 3), in which the permeability of real cracked zone is identical to the natural fracture. One of the simplest techniques to model the flow through a natural fracture is based on the parallel plate model. This is the only fracture model for which an exact calculation of the hydraulic conductivity is possible; this calculation yields the well-known 'cubic law' (Witherspoon et al. 1980). The derivation of the cubic law begins by assuming that the fracture walls can be represented by two smooth, parallel plates with infinite dimensions, separated by an aperture w. However, the real fractures have finite sizes, rough walls and variable apertures. It was shown that the parallel plate model is inadequate to describe the flow in natural fractures (Sisavath et al. 2003).

For a natural fracture, the aperture can generally be defined as mechanical (geometrically measured), or hydraulic (measured by analysis of the fluid flow). The mechanical joint aperture w is defined as the average point-to-point distance between two points of surfaces, perpendicular to the selected plane. The hydraulic aperture e can be determined from laboratory fluid-flow experiments. An important distinction has to be made between the theoretical smooth wall hydraulic aperture e and the real mechanical aperture w (geometrically measured) between two irregular joint walls. Owing to the wall friction and the tortuosity, w is generally larger than e. An empirical model was proposed by Barton et al. (1985) relating the hydraulic aperture e to the real mechanical aperture w and the joint roughness JRC. This relationship was defined based on the experimental data as

$$e = \frac{w^2}{JRC^{2.5}} \tag{24}$$

where e and w are expressed in micro-metres. It must be noted that this equation is only valid for $w \geq e$. The roughness of the crack surface depends on the toughness and size of aggregates and the properties of matrix and interface. It is assumed that the hydraulic aperture for cohesive zone is a function of w which is zero at the fictitious crack tip and equal to $\delta_c^2/JRC^{2.5}$ at real crack tip. This function can be defined via the experimental data. Based on the hydraulic aperture in the fractured zone, the longitudinal permeability coefficient k_l can be expressed as $e^2/12\,\mu$, with μ denoting the dynamic viscosity.

5 Numerical simulation results

In order to demonstrate a part of the wide range of problems that can be solved by the present approach, we have illustrated the performance of proposed computational algorithm in modeling of fracture propagation in partially saturated porous media. The finite element model is applied in partially saturated porous media and the cohesive interface elements are employed in the fractured zone where the cohesive tractions develop. The implementation of cohesive fracture elements is illustrated due to fluid flow inside the crack and the values of crack mouth opening are obtained as the crack proceeds. The first two examples are selected to illustrate the robustness and accuracy of computational algorithm for two benchmark problems. The first example deals with the drainage of water from a vertical column of sand to present the accuracy of proposed computational algorithm against the experimental results conducted by Liakopoulos (1965). The second example illustrates the performance of cohesive fracture elements for the simulation of hydraulically driven fracture propagation in poroelastic media against an analytical solution by Spence and Sharp (1985) and its numerical evaluation by Boone and Ingraffea (1990). Finally, the last example is chosen to demonstrate the capability of proposed model for the wedge splitting test performed by Slowik and Saouma (2000) at different rates of crack mouth opening.

5.1 Water drainage from a column of sand

The first example is chosen to evaluate the accuracy of computational modeling for the drainage of water from a vertical column of sand with those experimentally obtained by Liakopoulos (1965) and numerically reported by Lewis and Schrefler (1998). The problem was considered by various researchers

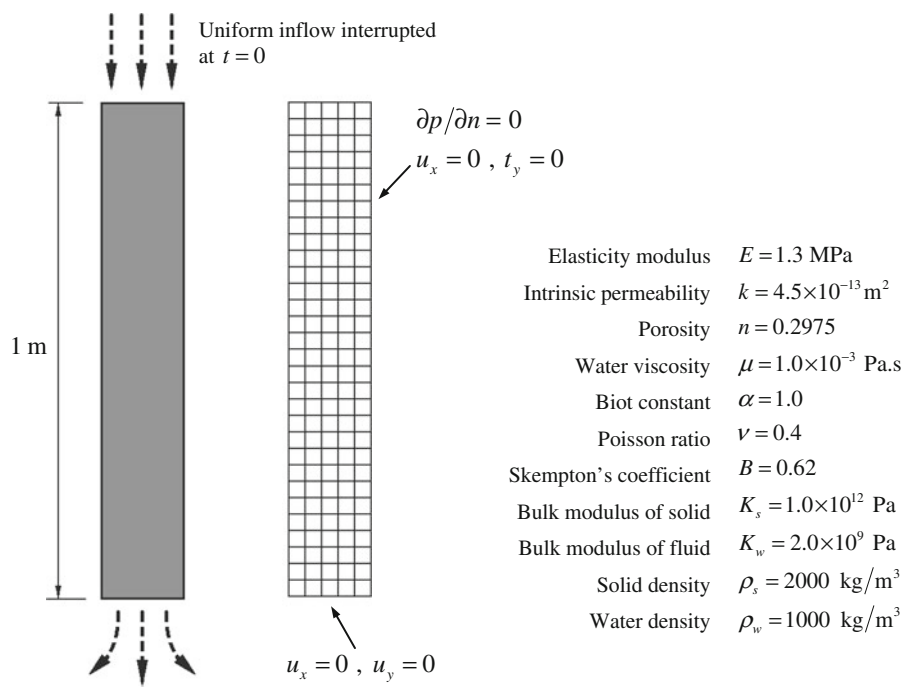

Fig. 4 The drainage of water from a vertical column of sand; The geometry, boundary conditions and material properties

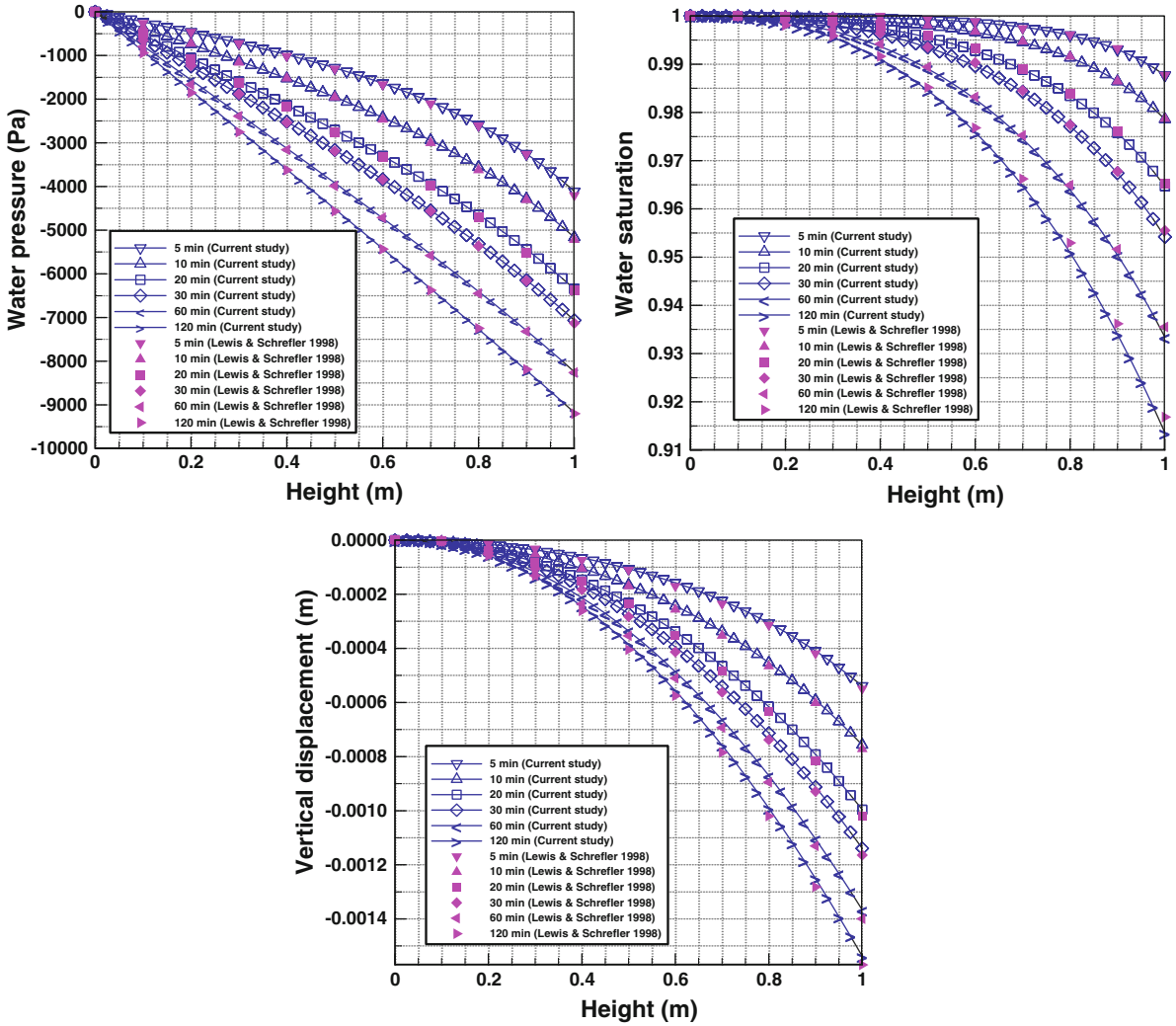

Fig. 5 Comparison of the numerical simulation results obtained by the present study and those reported by Lewis and Schrefler (1998) for water drainage from a *vertical column* of sand; variations of the water pressure (Pa), water saturation, and vertical displacement (m) versus column height

to verify their numerical analysis, and referred as a representative of wide range of problems involving gravity-governed partially saturated porous media since no external loads are applied. A perspex column of 1 m high is packed with sand and instrumented with tension-meters to measure the moisture tension at various points within the column. In order to apply the initial boundary conditions of laboratory test, water is added continuously from the top of column and is allowed to drain freely at the bottom through a filter, as shown in Fig. 4. The flow is carefully regulated until the tension-meters read zero pore pressure. At this stage, the inflow of water from the top is stopped and the upper boundary is made impermeable to water as an initial boundary condition. From then the tension-meter readings are recorded. The assumed material properties of sand together with the geometry and boundary conditions of the problem are shown in Fig. 4. In Fig. 5, the numerical results of partially saturated model for the water pressure, water saturation, and vertical displacement distribution versus the column height are presented for different times of 5, 10, 20, 30, 60 and 120 min. Clearly, it can be seen that the numerical results are in complete agreement with those reported by Lewis and Schrefler (1998). Figure 6 presents the time history of outflow rate at the

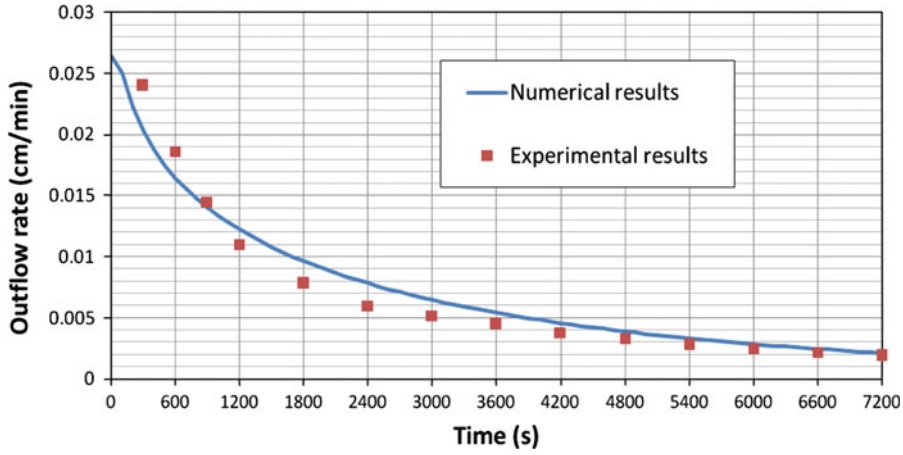

Fig. 6 The outflow rate at the *bottom of column* compared to the experimental data given by Liakopoulos (1965)

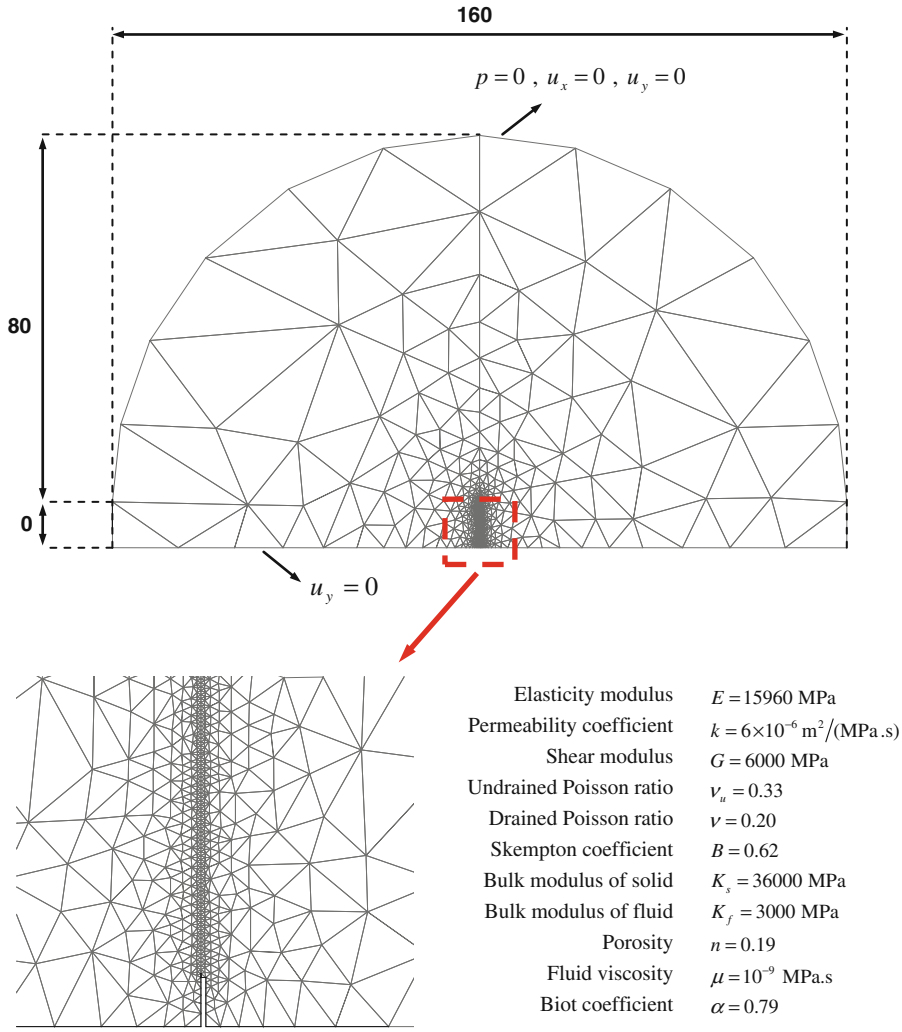

Fig. 7 The hydraulic fracture problem; The geometry and boundary conditions

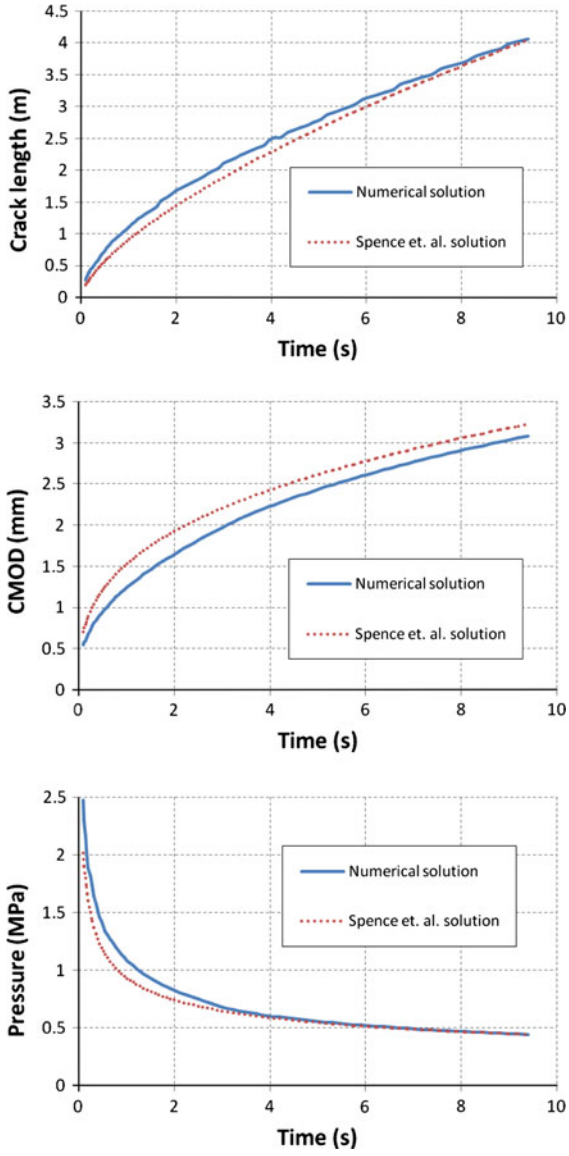

Fig. 8 The variations with time of the crack length, crack mouth opening (CMOD), and pressure distribution along crack mouth with those reported by Spence and Sharp (1985)

base of column. Obviously, the outflow rate gradually decreases to zero with time after stopping the inflow of water from the top at time $t = 0$. The curve shows a good agreement between the numerical results and experimental data given by Liakopoulos (1965).

5.2 Hydraulic fracturing

The second example illustrates the performance of cohesive fracture elements for the simulation of hydraulically driven fracture propagation in poroelastic media. This example is chosen here since the leakage flux into the surrounding porous media across the fracture border is important in hydraulic fracture modeling. An analytical solution was obtained for this example by Spence and Sharp (1985) and the numerical simulation by Boone and Ingraffea (1990), in which a finite element method was applied for the mechanical problem and a finite difference method for the flow analysis through the fracture. In Fig. 7, the geometry, boundary conditions and finite element mesh of the problem are presented together with the material properties. An initial crack is assumed at the borehole where the crack propagates, and a constant flow rate of 0.0001 m^3/s is applied at the crack mouth. The crack propagates when the principle effective stress at crack tip reaches the ultimate tensile strength of the material assumed to be 0.5 MPa.

The length of cohesive elements is chosen so that the fracture process zone is discretized with adequate resolution and the need for numerical convergence is satisfied. The length of process zone R_c can be approximated by $R_c = \eta E' G_f / f_t'^2$ (Bazant and Planas 1998), where G_f is the specific fracture energy, f_t' the tensile strength, η a constant equal to $\pi/8$ according to Barenblatt cohesive theory, and E' the effective elastic modulus defined as E for plane stress and $E/(1-\upsilon^2)$ for plane strain problems. The limiting values for the size of a fully developed fracture process zone range from 0.3 to 2 m for concrete and similar quasi-brittle materials. For a brittle material, it is generally argued that 2–5 elements are necessary to resolve the cohesive zone (Zhou et al. 2005). By evaluating the process zone length and determining the cohesive elements length, a uniform mesh is generated in the area surrounding the crack. The mesh uniformity is ascertained by local remeshing in this area. In addition, a rosette configuration with uniform elements around crack tip is constructed by adding new boundaries around the crack tip. The random orientation of elements is gained by using a Delaunay based unstructured grid generator (Khoei et al. 2008). It is assumed that the crack propagation takes place according to Dugdale (1960) and Barenblatt (1962) cohesive models, in which the traction principle effective stress at crack tip reaches the ultimate tensile strength of the material.

Figure 8 presents the variations with time of the crack length, crack mouth opening (CMOD), and pressure distribution along crack mouth. The results of numerical simulations are compared with those reported by

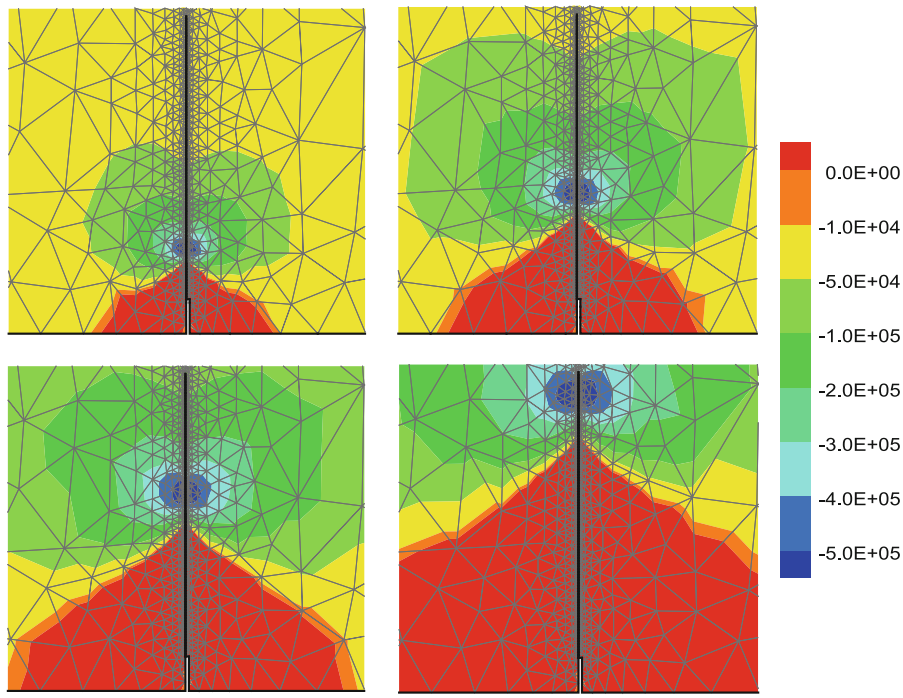

Fig. 9 The distribution of maximum principal effective stress contours at various time steps $t = 2.0, 4.0, 6.0$ and 9 s

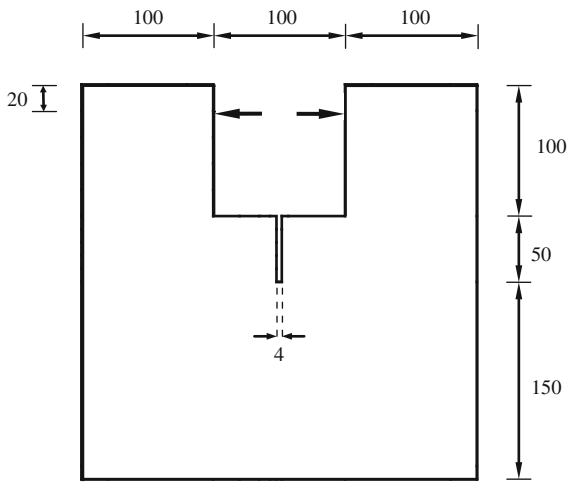

Fig. 10 The specimen geometry and boundary conditions (all dimensions in mm)

Spence and Sharp (1985). A good agreement can be observed between two different simulations. In Fig. 9, the distribution of maximum principal effective stress contours are presented at $t = 2.0, 4.0, 6.0$ and 9 s.

5.3 The wedge splitting test

The last example demonstrates the capability of proposed computational model for the wedge splitting test performed experimentally by Slowik and Saouma (2000). The geometry and boundary conditions of specimen are shown in Fig. 10. The water input pressure is applied only at notch section while zero pressure is assumed at the rest of boundary. Two different rates are used for the crack mouth opening displacement (CMOD), including the slow crack opening with the rate of 2 μm/s and the fast crack opening with the rate of 200 μm/s. It is well known that the higher velocity of crack mouth opening may develop extra micro-cracks within the crack tip zone since they have no time to unload each other. As a result, due to fast growth of the main crack, several micro-cracks may be formed at the main crack tip zone that dissipates more energy. Although the multi-microcracking process in the fast crack growth may result in the increase of local stress, this stress increase is less important compared to the increase of fracture energy. It was assumed by Bazant and Li (1997a,b) that the normalized effective stress—displacement ($\sigma_c - \delta_c$) curve expands outwards when the cohesive opening rate increases. It was also shown by Zhou and Molinari (2004) that the failure strength of ceramic increases by 10–15% when the strain rate increases 125 times. Hence, it can be concluded that both σ_c and δ_c increase with the increase of crack velocity.

Table 1 The material parameters for concrete

Material properties	Fast loading	Slow loading
Elasticity modulus (MPa)	25,000	25,000
Poisson ratio	0.17	0.17
Density of solid particles (kg/m^3)	2,720	2,720
Water density (kg/m^3)	1,000	1,000
Tensile strength (MPa)	1.32	1.25
Critical displacement δ_c (mm)	0.25	0.2
Permeability (m^2/Pa s)	10^{-15}	10^{-15}
Prosity	0.1	0.1
Bulk modulus of solid (MPa)	36,000	36,000
Bulk modulus of fluid (MPa)	3,000	3,000
Fluid viscosity (MPa s)	10^{-9}	10^{-9}

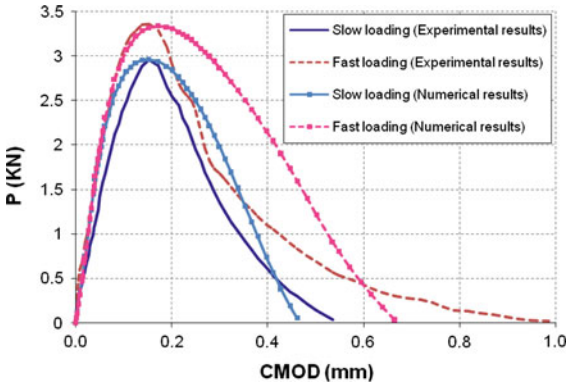

Fig. 11 The load versus CMOD for the slow and fast loading; A comparison between the numerical results and experimental data

The material properties employed for experimental tests in the case of fast and slow loading rates are given in Table 1. It has been observed from numerical simulations that the increase of micro-cracks due to fast loading rate increases the permeability of fracture process zone. It is obtained that in the slow loading rate, the Barton model with JRC equal to 20 satisfactorily predicts the hydraulic aperture for the entire of fracture, however—using this relation for the fast loading rate leads to the lower pressure through the fracture path in comparison with the experimental data. It is also observed that a linear function between the hydraulic and mechanical apertures improves the results effectively in the fracture process zone although the quadratic function was proposed by Barton et al. (1985).

In Fig. 11, the variations of applied force with crack mouth opening displacement (CMOD) are plotted for both experimental and numerical results of the wedge splitting test in the case of slow and fast loading rates at the water input pressure of 0.21 MPa. Figure 12 presents the experimentally and numerically variations of pressure distributions along the

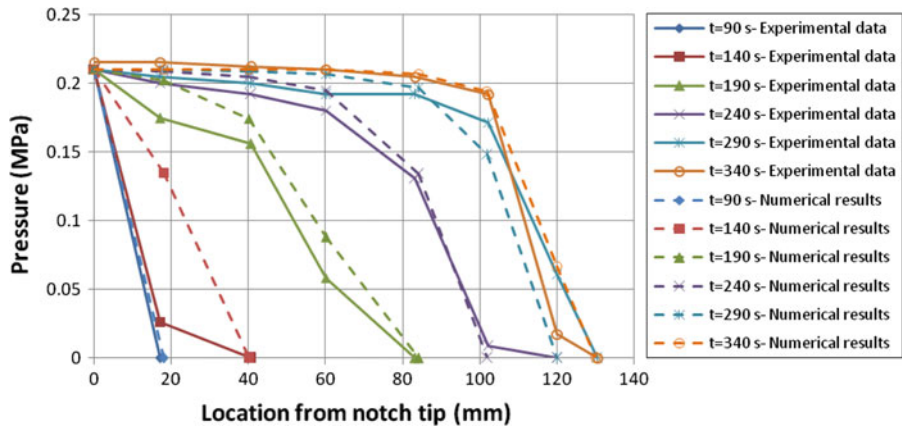

Fig. 12 A comparison between numerical and experimental results of water pressure variations for slow loading at various time steps using the input pressure of 0.21 MPa

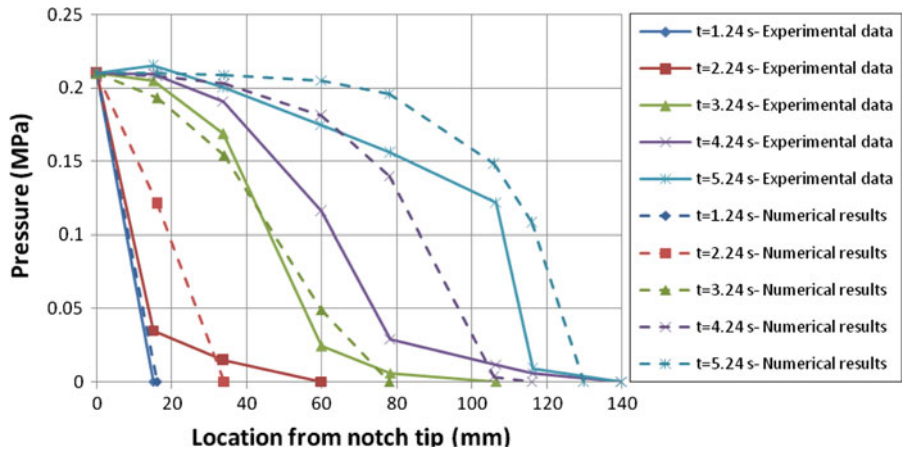

Fig. 13 A comparison between numerical and experimental results of water pressure variations for fast loading at various time steps using the input pressure of 0.21 MPa

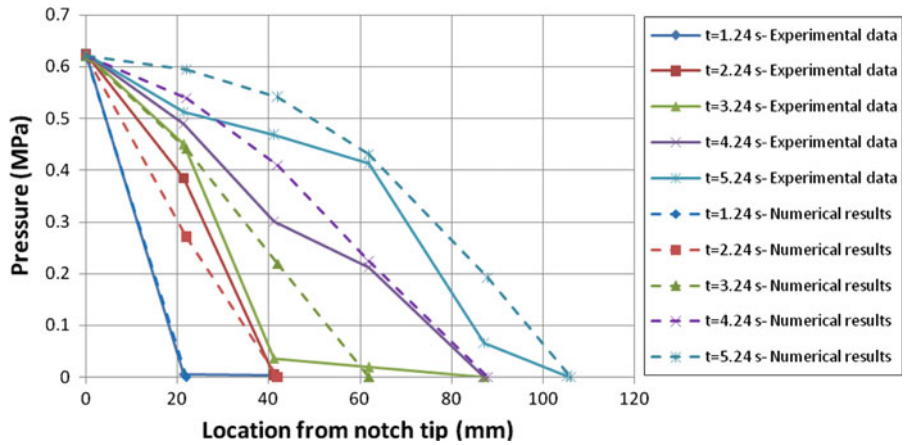

Fig. 14 A comparison between numerical and experimental results of water pressure variations for fast loading at various time steps using the input pressure of 0.62 MPa

crack path for different time steps in the case of slow loading rate at the water input pressure of 0.21 MPa. Also plotted in Fig. 13 are the variations of pressure distributions along the crack path for the fast loading rate. In Fig. 14, the experimental and numerical results of pressure distributions are depicted for various time steps in the case of fast loading rate at the water input pressure of 0.62 MPa. Obviously, good agreements can be seen between the experimental and numerical results. The results indicate that the proposed permeability properly predict the fluid flow through the fracture zone. In Fig. 15, the distribution of effective stress σ_x' contours are shown at time steps $t = 0.2, 0.86, 2.24$ and 3.24 s for the fast loading rate at the water input pressure of 0.21 MPa. Finally, the variations of normal cohesive traction along the fracture length are plotted in Fig. 16 at the water input pressure of 0.21 MPa. This example clearly presents the effect of crack mouth opening rates in the wedge splitting test using a modified permeability to consider the roughness of fracture walls.

It is worth mentioning that when the crack propagates in an opening mode, the water flows in the crack front region provided by the tensile strain due to external loading applied to the specimen. This region may be impermeable for water phase at the initial stage of loading because of narrow channels to flow. However, by increasing the tensile strain the channel is wide enough for water to flow in it. Due to high compressibility of gas, small volume of gas, and connectivity of pore network, it is a reasonable assumption to set the gas pressure equal to zero. The numerical results of above example confirm this assumption and show that the fracture permeability can be modeled appropriately considering fracture wall roughness. However, it could be important to consider the gas pressure in the crack front region for the fracture closing mode.

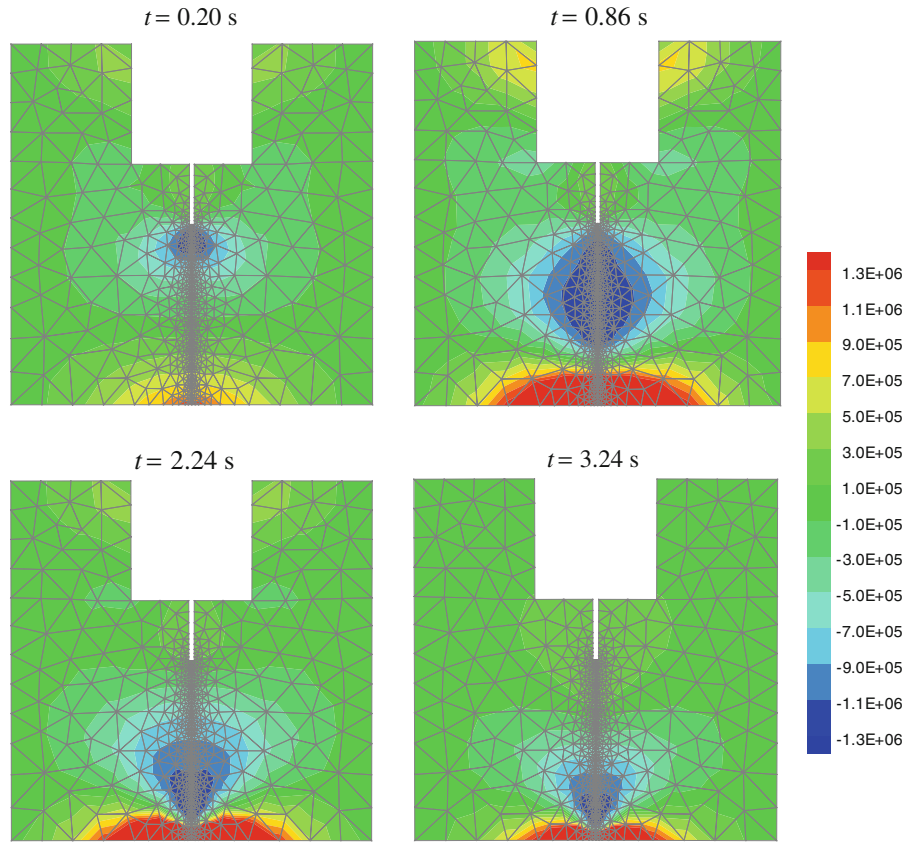

Fig. 15 The distribution of effective stress σ'_x contours at various time steps for fast loading using the input pressure of 0.21 MPa (all dimensions in Pa), Compression assumed to be positive

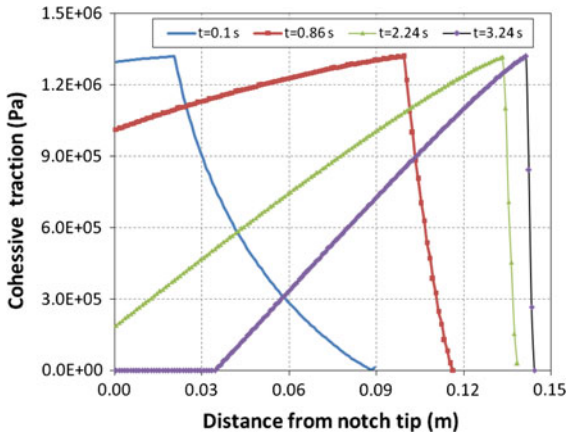

Fig. 16 The variations of normal cohesive traction along the fracture length at various time steps for the input pressure of 0.21 MPa

6 Conclusion

In the present paper, a finite element model was presented for the numerical simulation of cohesive fracture in partially saturated porous media. The double-nodded zero-thickness cohesive interface element was employed to represent the mixed mode fracture behavior in tension and compression. In order to describe the behavior of fractured media, two equilibrium equations were applied similar to those employed for the mixture of solid–fluid phase in partially saturated media, including: the momentum balance of fractured media, and the balance of fluid mass within the fracture. Finally, three numerical simulations were performed to demonstrate a part of the wide range of problems that can be solved by the present computational algorithm. The first two examples, i.e. the water drainage from a vertical column of sand and the hydraulically driven fracture propagation in poro-elastic media, were chosen to illustrate the robustness and accuracy of computational algorithm for two benchmark problems. The third example was selected to present the effect of crack mouth opening rates in the wedge splitting test. Based on the experimental data, a modified fracture permeability was proposed for the fracture zone to consider the roughness of fracture walls. It has been shown that

for the slow loading rate the Barton model properly predict the pressure distribution along the crack path. However, a modified relation is necessary for the fast loading rate due to extra micro-cracks in the fracture process zone.

References

Alonso EE, Gens A, Josa A (1990) A constitutive model for partially saturated soils. Geotechnique 40:405–430

Barenblatt GI (1962) The mathematical theory of equilibrium cracks in brittle fracture. Adv Appl Mech 7:55–62

Baroghel-Bouny V, Mainguy M, Lassabatere T, Coussy O (1999) Characterization and identification of equilibrium and transfer moisture properties for ordinary and high-performance cementitious materials. Cem Conc Res 29:1225–1238

Barton N, Bandis S, Bakhtar K (1985) Strength, deformation and conductivity coupling of rock joints. Int J Rock Mech Min Sci Geomech Abstr 22:121–140

Bazant ZP, Li YN (1997a) Cohesive crack with rate-dependent opening and viscoelasticity: 1. Mathematical model and scaling. Int J Fract 86:247–265

Bazant ZP, Li YN (1997b) Cohesive crack with rate-dependent opening and viscoelasticity: 2. Numerical algorithm, behavior and size effect. Int J Fract 86:267–288

Bazant ZP, Planas J (1998) Fracture and size effect in concrete and other quasibrittle materials. CRC Press, New York

Biot MA (1941) General theory of three dimensional consolidation. J Appl Phys 12:155–164

Birgisson B, Montepara A, Romeo E, Roncella R, Napier JAL, Tebaldi G (2008) Determination and prediction of crack patterns in hot mix asphalt (HMA) mixtures. Eng Frac Mech 75:664–673

Boone TJ, Ingraffea AR (1990) A numerical procedure for simulation of hydraulically driven fracture propagation in poroelastic media. Int J Numer Analy Meth Geomech 14: 27–47

Brühwiler E, Saoma VE (1995a) Water fracture interaction in concrete. Part I: fracture properties. ACI Mater J 92:296–303

Brühwiler E, Saoma VE (1995b) Water fracture interaction in concrete. Part II: hydrostatic pressure in cracks. ACI Mater J 92:383–390

Camacho GT, Ortiz M (1996) Computational modeling of impact damage in brittle materials. Int J Solids Struct 33:2899–2938

Dugdale DS (1960) Yielding of steel sheets containing slits. J Mech Phys Solids 8:100–108

Gawin D, Schrefler BA (1996) Thermo-hydro-mechanical analysis of partially saturated porous materials. Eng Comput 13:113–143

Ghaboussi J, Wilson EL (1973) Flow of compressible fluid in porous elastic media. Int J Numer Methods Eng 5:419–442

Guiducci C, Pellegrino A, Radu JP, Collin F, Charlier R (2002) Numerical modeling of hydro-mechanical fracture behavior. In: Pande GN, Pietruszczak S (eds) Numerical models in geomechanics—NUMOG VIII. Swets & Zeitlinger, Amsterdam, pp 293–299

Hilleborg A, Modeer M, Petersson PE (1976) Analysis of crack formation and crack growth in concrete by means of fracture mechanics and finite elements. Cem Conc Res 6:773–782

Jenq Y, Shah SP (1991) Features of mechanics of quasi-brittle crack propagation in concrete. Int J Fract 51:103–120

Khoei AR (2005) Computational plasticity in powder forming processes. Elsevier, UK

Khoei AR, Azami AR, Haeri SM (2004) Implementation of plasticity based models in dynamic analysis of earth and rockfill dams: a comparison of Pastor-Zienkiewicz and cap models. Comput Geotech 31:385–410

Khoei AR, Gharehbaghi SA, Azami AR, Tabarraie AR (2006) SUT-DAM: an integrated software environment for multidisciplinary geotechnical engineering. Adv Eng Softw 37: 728–753

Khoei AR, Azadi H, Moslemi H (2008) Modeling of crack propagation via an automatic adaptive mesh refinement based on modified superconvergent patch recovery technique. Eng Fract Mech 75:2921–2945

Khoei AR, Moslemi H, Majd Ardakany K, Barani OR, Azadi H (2009) Modeling of cohesive crack growth using an adaptive mesh refinement via the modified–SPR technique. Int J Fract 159:21–41

Khoei AR, Barani OR, Mofid M (2010) Modeling of dynamic cohesive fracture propagation in porous saturated media. Int J Numer Anal Methods Geomech (in press)

Lewis RW, Schrefler BA (1998) The finite element method in the static and dynamic deformation and consolidation of porous media. John Wiley, New York

Liakopoulos AC (1965) Transient flow through unsaturated porous media. PhD thesis, University of California, Berkeley, CA

Meschke G, Grasberger S (2003) Numerical modeling of coupled hygromechanical degradation of cementitious materials. J Eng Mech 129:383–392

Ng KLA, Small JC (1997) Behavior of joints and interfaces subjected to water pressure. Comput Geotech 20:71–93

Ortiz M, Suresh S (1993) Statistical properties of residual stresses and intergranular fracture in ceramic materials. J Appl Mech 60:77–84

Persson B (1997) Moisture in concrete subjected to different kinds of curing. Mater Struct 30:533–544

Reinhardt HW, Sosoro M, Zhu X (1998) Cracked and repaired concrete subject to fluid penetration. Mater Struct 31:74–93

Rescher OJ (1990) Importance of cracking in concrete dams. Eng Fract Mech 35:503–524

Savage BM, Janssen DJ (1997) Soil physics principles validated for use in predicting unsaturated moisture movement in portland cement concrete. ACI Mater J 94:63–70

Schrefler BA, Secchi S, Simoni L (2006) On adaptive refinement techniques in multi-field problems including cohesive fracture. Comput Methods Appl Mech Eng 195:444–461

Secchi S, Simoni L, Schrefler BA (2007) Mesh adaptation and transfer schemes for discrete fracture propagation in porous materials. Int J Numer Anal Methods Geomech 31: 331–345

Segura JM, Carol I (2004) On zero-thickness elements for diffusion problems. Int J Numer Anal Methods Geomech 28:947–962

Shum KM, Hutchinson JW (1990) On toughening by Micro-Cracks. Mech Mat 9:83–91

Simoni L, Secchi S (2003) Cohesive fracture mechanics for a multi-phase porous medium. Eng Comput 20:675–698

Sisavath S, Al-Yaarubi A, Pain C, Zimmerman RW (2003) A simple model for deviation from the cubic law for a fracture undergoing dilation or closure. Pure Appl Geophys 160:1009–1022

Slowik V, Saouma VE (2000) Water pressure in propagating concrete cracks. J Struct Eng ASCE 126:235–242

Song SH, Paulino GP, Buttlar WG (2006) A bilinear cohesive zone model tailored for fracture of asphalt concrete considering viscoelastic bulk material. Eng Fract Mech 73:2829–2848

Spence DA, Sharp P (1985) Self-similar solutions for elasto-hydrodynamic cavity flow. Proc Royal Soc London A 400:289–313

van Genuchten M (1980) A closed-form equation for predicting the hydraulic conductivity of unsaturated soil. Soil Sci Soc Am J 44:892–898

Witherspoon PA, Wang JSY, Iwai K, Gale JE (1980) Validity of cubic low for fluid flow in a deformable rock fracture. Water Resour Res 16:1016–1024

Xu XP, Needleman A (1994) Numerical simulations of fast crack growth in brittle solids. J Mech Phys Solids 42:1397–1434

Zhou F, Molinari JF (2004) Stochastic fracture of ceramics under dynamic tensile loading. Int J Solids Struct 41:6573–6596

Zhou F, Molinari JF, Shioya T (2005) A rate-dependent cohesive model for simulating dynamic crack propagation in brittle materials. Eng Fract Mech 72:1383–1410

Zhu X, Pekau OA (2007) Seismic behavior of concrete gravity dams with penetrated cracks and equivalent impact damping. Eng Struct 29:336–345

Zienkiewicz OC, Xie YM, Schrefler BA, Ledesma A, Bicanic N (1990) Static and dynamic behavior of soils; a rational approach to quantitative solution. Part II. Semi-saturated problems. Proc Royal Soc London 311–321

Zienkiewicz OC, Chan AHC, Pastor M, Schrefler BA, Shiomi T (1999) Computational geomechanics with special reference to earthquake engineering. Wiley, London